

# Piperazine-derived lipid nanoparticles deliver mRNA to immune cells in vivo

Received: 16 December 2021

Accepted: 22 July 2022

Published online: 15 August 2022

 Check for updates

Huanzhen Ni<sup>1,6</sup>, Marine Z. C. Hatit<sup>1,6</sup>, Kun Zhao<sup>1,5,6</sup>, David Loughrey<sup>1</sup>, Melissa P. Lokugamage<sup>1</sup>, Hannah E. Peck<sup>2</sup>, Ada Del Cid<sup>1</sup>, Abinaya Muralidharan<sup>3,4</sup>, YongTae Kim<sup>1,2,3,4</sup>, Philip J. Santangelo<sup>1</sup> & James E. Dahlman<sup>1</sup>✉

In humans, lipid nanoparticles (LNPs) have safely delivered therapeutic RNA to hepatocytes after systemic administration and to antigen-presenting cells after intramuscular injection. However, systemic RNA delivery to non-hepatocytes remains challenging, especially without targeting ligands such as antibodies, peptides, or aptamers. Here we report that piperazine-containing ionizable lipids (Pi-Lipids) preferentially deliver mRNA to immune cells in vivo without targeting ligands. After synthesizing and characterizing Pi-Lipids, we use high-throughput DNA barcoding to quantify how 65 chemically distinct LNPs functionally delivered mRNA (i.e., mRNA translated into functional, gene-editing protein) in 14 cell types directly in vivo. By analyzing the relationships between lipid structure and cellular targeting, we identify lipid traits that increase delivery in vivo. In addition, we characterize Pi-A10, an LNP that preferentially delivers mRNA to the liver and splenic immune cells at the clinically relevant dose of 0.3 mg/kg. These data demonstrate that high-throughput in vivo studies can identify nanoparticles with natural non-hepatocyte tropism and support the hypothesis that lipids with bioactive small-molecule motifs can deliver mRNA in vivo.

The Food and Drug Administration (FDA) approved its first lipid nanoparticle (LNP)-based siRNA drug to treat an inherited genetic disease in 2018<sup>1</sup>. Since then, systemically administered siRNA therapeutics using N-acetylgalactosamine<sup>2</sup> have been approved to treat additional liver diseases<sup>3–5</sup>. Similarly, intramuscularly administered mRNA therapies have been FDA approved<sup>6,7</sup> to vaccinate against coronavirus disease in 2019. Unfortunately, there have also been clinical failures potentially driven by insufficient delivery<sup>8,9</sup>. Taken together, the efficacy of approved RNA vaccines and liver therapies underscores the potential clinical impact of LNPs with tropism to new cell types.

Delivering RNA to non-hepatocytes<sup>10,11</sup> has remained challenging in large part due to the anatomy and physiology of the liver. Specifically, the hepatic sinusoids contain a discontinuous vasculature<sup>12</sup> as

well as slow blood flow<sup>13</sup>; both increase nanoparticle extravasation and subsequent interactions with hepatocytes. To target non-hepatocytes, scientists have used three approaches<sup>14</sup>. The first is to pre-treat animals with systems that overwhelm the liver<sup>15</sup> or reduce drug activity<sup>16</sup> in specific cell types, thereby shifting tropism. However, it remains unclear whether this multistep strategy has clinical relevance. In the second approach, an LNP with tropism to hepatocytes is retargeted with an active targeting ligand. For example, LNPs made with DLin-MC3-DMA<sup>17</sup>, an ionizable lipid that is FDA approved for hepatocyte siRNA delivery<sup>18</sup>, have been retargeted to immune cells using a lipid-bound antibody<sup>19–22</sup>. One potential limitation of this approach is that actively targeted nanoparticles containing RNA drugs have led to adverse events in clinical trials<sup>23</sup>; one important caveat is that these

<sup>1</sup>Wallace H. Coulter Department of Biomedical Engineering, Georgia Institute of Technology, Atlanta, GA, USA. <sup>2</sup>Parker H. Petit Institute for Bioengineering and Bioscience, Georgia Institute of Technology, Atlanta, GA, USA. <sup>3</sup>George W. Woodruff School of Mechanical Engineering, Georgia Institute of Technology, Atlanta, GA, USA. <sup>4</sup>Institute for Electronics and Nanotechnology, Georgia Institute of Technology, Atlanta, GA, USA. <sup>5</sup>Present address: School of Pharmaceutical Sciences, Shandong University, Jinan, China. <sup>6</sup>These authors contributed equally: Huanzhen Ni, Marine Z. C. Hatit, Kun Zhao.

✉ e-mail: [james.dahlman@bme.gatech.edu](mailto:james.dahlman@bme.gatech.edu)

were not LNPs. In a third approach, scientists identify nanoparticles that interact with natural trafficking pathways, thereby leading to endogenous targeting<sup>24</sup>. Although these approaches have led to an FDA approval<sup>18</sup> and promising phase I clinical data<sup>25</sup>, this approach also has a key limitation. After synthesizing a large, chemically diverse lipid library, scientists must evaluate how each nanoparticle delivers its payload into cells. Since injecting and sacrificing thousands of mice per library is unethical, this screening is performed *in vitro* (i.e., in cell culture). For example, across three representative papers<sup>26–28</sup>, labs tested 4,736 nanoparticles *in vitro*, using the data to select 14 nanoparticles for *in vivo* studies. However, this screening method is likely inefficient, given that *in vitro* nanoparticle delivery can be a poor predictor of *in vivo* nanoparticle delivery<sup>29</sup>.

One potential solution to this problem is to study many nanoparticles in a single animal, which has recently become feasible using DNA-barcoded nanoparticles<sup>30, 31</sup>. Here we use Fast Identification of Nanoparticle Delivery (FIND)<sup>32</sup>, a DNA barcode-based high-throughput LNP screening system, to characterize how 65 chemically distinct LNPs functionally deliver gene-editing mRNA to 14 cell types *in vivo*. FIND allowed us to test a chemical hypothesis directly *in vivo*: that medicinal chemistry scaffolds with known bioactivity could be incorporated into the ionizable lipids used in LNPs. We reasoned that these motifs could lead to distinctive *in vivo* activity, compared to canonical motifs used in many LNPs to date. We therefore focused on piperazine, a six-membered nitrogen-containing heterocycle, for several reasons. First, piperazine is commonly used in biologically active compounds<sup>33</sup>; 13 of the 200 best-selling small-molecule drugs in 2012 contained a piperazine ring<sup>34</sup>. Second, and relatedly, the piperazine ring has been recognized as the key structural motif in marketed drugs ranging from antidepressants<sup>35, 36</sup> to antibiotics<sup>37, 38</sup>, demonstrating its utility in medicinal chemistry. Third, as a result of piperazine's impact on small-molecule drugs, there are numerous piperazine-based chemistries<sup>34</sup> that could be repurposed to synthesize diverse ionizable lipids.

## Results

We first rationally designed ionizable lipids consisting of a piperazine core and two tertiary amines as ionizable headgroups linked to hydrophobic carbon chains, which we termed “Pi-Lipids” (Fig. 1a). We originally chose ester bonds as linkers; however, this synthetic strategy did not afford the expected compounds. We therefore switched to an amide bond. To the piperazine core, we added a saturated hydrocarbon chain ranging from C10 to C12 in our design. We chose this lipid length since C8 to C12 lipids are well represented among other lead ionizable lipids<sup>26, 39</sup> and may help to disrupt cellular membranes, thereby facilitating delivery<sup>40</sup>. Finally, since it was shown that linoleate chains enhanced LNP delivery<sup>41</sup>, we added linoleate-based scaffolds to our design. We successfully synthesized eight novel piperazine-based ionizable lipids (Fig. 1b, c). Briefly, a simple and straightforward amide coupling reaction between 1,4-bis(3-aminopropyl)piperazine and Boc-protected  $\beta$ -Alanine or  $\gamma$ -Aminobutyric acid yielded piperazine intermediates, in 12 h, with a 50% yield. A subsequent Boc deprotection followed by a one-pot reductive amination reaction with different hydrophobic aldehydes led to the final piperazine-based lipids (PPZ) in yields of 32 to 59%. We varied the length of the carbon chain linkage and synthesized lipids in two scaffolds, PPZ-A containing two carbons as linkage and PPZ-B containing three carbons. The lipid structures were confirmed by nuclear magnetic resonance (NMR) and high-resolution mass spectrometry (HRMS) (see supporting information) (Fig. 1b).

### PPZ lipids formulate into stable lipid nanoparticles with mRNA

We then investigated whether novel Pi-Lipids formulated into stable, monodisperse LNPs, which we termed Pi-LNPs. LNPs are typically formulated using four components: (i) an ionizable or cationic lipid, (ii) a PEG-lipid, (iii) a cholesterol, and (iv) a helper lipid. Thus, to isolate the

effect of the Pi-Lipids, we formulated the LNPs with components that were previously shown to form stable LNPs with other (i) ionizable or cationic lipids. Specifically, we chose (ii) two PEG-lipids with different lengths of carbon chains (C<sub>14</sub>PEG<sub>2K</sub> and C<sub>18</sub>PEG<sub>2K</sub>), (iii) two cholesterol variants (cholesterol, 20 $\alpha$ -OH cholesterol), and (iv) 1,2-dioleoyl-sn-glycerol-3-phosphoethanolamine (DOPE) (Fig. 1b, c). Since LNP formation and stability can vary with the ratio of these four components, we added a control to ensure our results were robust, testing four different molar ratios (Fig. 1d). Thus, using microfluidics<sup>42</sup>, we formulated 128 chemically distinct Pi-LNPs.

We analyzed Pi-LNPs using a FIND<sup>32</sup>, a DNA barcode-based assay that quantifies how dozens of different LNPs deliver mRNA *in vivo*<sup>43–45</sup>. We formulated LNP 1, with chemical composition 1, to carry Cre mRNA and DNA barcode 1, and LNP N, with chemical composition N, to carry Cre mRNA and DNA barcode N. By incorporating a distinct DNA barcode in each LNP, we were able to identify individual LNP delivery through deep sequencing. We performed a quality control step, quantifying the hydrodynamic diameter and polydispersity of all 128 Pi-LNPs individually using dynamic light scattering. Only monodisperse Pi-LNPs with diameters from 20 nm to 200 nm, measured by intensity average, were selected. Of the original 128 Pi-LNPs, 65 met these criteria and were pooled together for subsequent *in vivo* administration (Fig. 1d, e).

To understand the effect of chemical structure on Pi-LNP formation, we analyzed the hydrodynamic diameters, observing that lipids with shorter C10 carbon chains formed Pi-LNPs with an average diameter of 96 nm for PPZ-A10 and 100 nm for PPZ-B10. By contrast, lipids with longer carbon chains (C<sub>18</sub>) formed LNPs with larger diameters, including 134 nm for PPZ-A18-2Z and 155 nm for PPZ-B18-2Z (Fig. 1f). We found that while the Pi-LNP diameter did seem to vary with the structure of the Pi-Lipid, the diameter did not change as a function of the cholesterol (Fig. 1g). Finally, we tested the diameter of the pool of Pi-LNPs and found it within the range of the diameters of the 65 Pi-LNPs, suggesting that mixing the Pi-LNPs did not cause them to come out of the solution (Fig. 1h). Taken together, these data led us to conclude that Pi-Lipids can form monodisperse, stable Pi-LNPs.

After characterizing the pool of 65 Pi-LNPs, we intravenously injected them in Ai14 mice at a total nucleic dose of 1.5 mg/kg (averaging a 0.023 mg total nucleic acid/kg/particle, for all 65 Pi-LNPs) (Fig. 2a). The Ai14 mice have a Lox-Stop-Lox-tdTomato construct downstream of a CAG promoter. Thus, if Cre mRNA is delivered into a target cell and is subsequently functionally translated into Cre protein, the cells become tdTomato+ (Fig. 2a). By isolating tdTomato+ cells using fluorescence-activated cell sorting (FACS) (Supplementary Figs. 1 and 2) and sequencing the cells using next-generation sequencing, we can isolate the DNA barcodes, associated with specific LNPs, within cells that were functionally transfected with Cre mRNA<sup>32, 43–45</sup>. Three days after injection, we isolated the liver, spleen, lung, and kidney and quantified the percentage of tdTomato+ cells from 14 different cell populations (Fig. 2b). We observed 40% of tdTomato+ cells in Kupffer cells, 10% in spleen macrophages, and 16% in spleen dendritic cells. The percentage of tdTomato+ quantified in liver endothelial cells and dendritic cells was < 5%, and we did not observe any delivery in the lung and kidney. After isolating tdTomato+ cells from the most targeted cell populations—Kupffer cells, spleen macrophages, and dendritic cells—we investigated how well each of the 65 LNPs performed using next-generation DNA sequencing. From the barcode raw counts obtained through sequencing, we calculated the normalized delivery of each individual barcode. Briefly, the normalized delivery of a given barcode is calculated as the number of counts for that barcode divided by the counts for all N barcodes (Supplementary Fig. 3). This allowed us to identify barcodes that were preferentially delivered to specific cell types, which then directed us to LNPs carrying those barcodes. As a control, we quantified unencapsulated barcodes, which were also injected. Since unprotected DNA does not readily enter cells, its

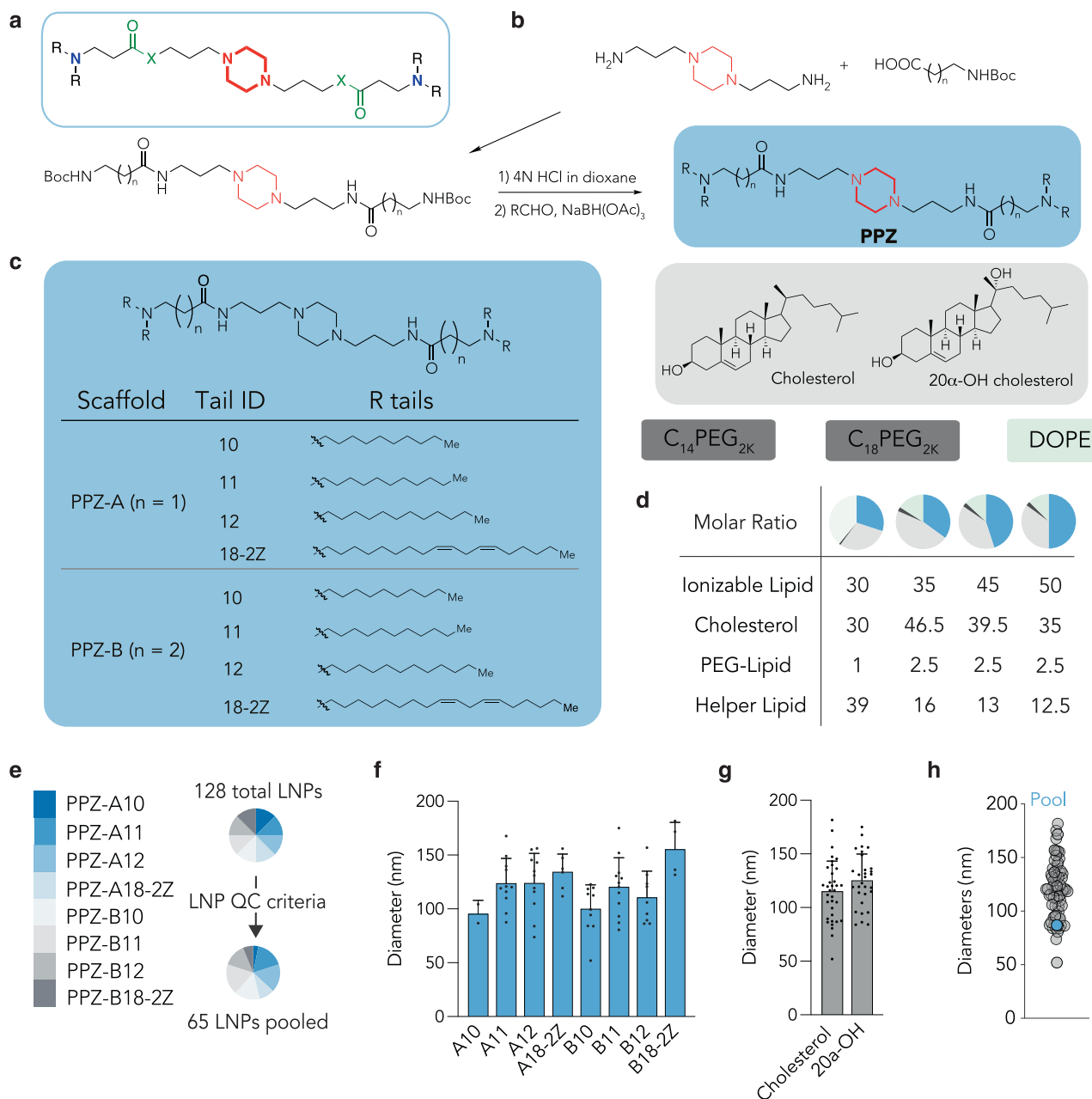


**Fig. 1 | Piperazine-based lipids formulate into stable lipid nanoparticles (LNPs).**

**a** Design of ionizable lipids with piperazine backbone. **b** Procedure to synthesize PPZ lipids. **c** Composition of the LNP library: 8 different PPZ lipids, 2 cholesterol variants (cholesterol and 20 $\alpha$ -OH cholesterol), 2 PEG-lipid variants (C<sub>14</sub>PEG<sub>2K</sub> and C<sub>18</sub>PEG<sub>2K</sub>), and DOPE. **d** Each of the compounds was formulated using four molar ratios. **e** Of the 128 LNPs that were formulated, 65 passed the quality control

criteria, with a diameter less than 200 nm as well as a stable autocorrelation curve. **f** Hydrodynamic diameters of LNPs formulated with PPZ lipids, average  $\pm$  SEM. **g** Hydrodynamic diameters of LNPs formulated with cholesterol and 20 $\alpha$ -OH cholesterol, average  $\pm$  SEM. **h** Hydrodynamic diameters of all administered LNPs; the diameter of the LNP pooled control is within the range of the LNPs composing the pool.

normalized delivery is expected to be the lowest among all the barcodes<sup>30</sup>, which was the case when the barcodes were calculated across all cell types (Fig. 2c).

### Understanding LNP properties and tropism with PPZ lipids

We then used this large dataset to perform a comprehensive in vivo structure-function analysis across all cell types. First, we analyzed the averaged normalized delivery of LNPs based on different Pi-Lipid structures and found that Pi-LNPs containing PPZ-A10 exhibited the highest delivery, followed by Pi-LNPs formulated with PPZ-A11 (Fig. 2d). We hypothesized that the difference in normalized delivery observed between Pi-LNPs could be due to disparities in encapsulation efficiency or LNP diameters. To test this hypothesis,

we formulated eight LNPs varying only the ionizable lipid structure while keeping the same molar ratio and compound compositions and measured both the diameter and encapsulation efficiency for each LNP (Fig. 2e). Interestingly, we observed an increase in the encapsulation efficiency from 66 to 88% for Pi-LNPs formulated with PPZ-A10 to PPZ-A18-2Z, respectively, suggesting that the encapsulation efficiency increases with longer carbon chains. However, Pi-LNPs with longer carbon chains also displayed large diameters between 150 and 300 nm, which is unfavorable for LNP delivery<sup>46</sup>. Encapsulation efficiencies between Pi-LNPs formulated with PPZ-A and PPZ-B lipids were comparable, but large diameters were observed for Pi-LNPs containing PPZ-B lipids, potentially explaining the reduced delivery observed for those compounds (Fig. 2d). To

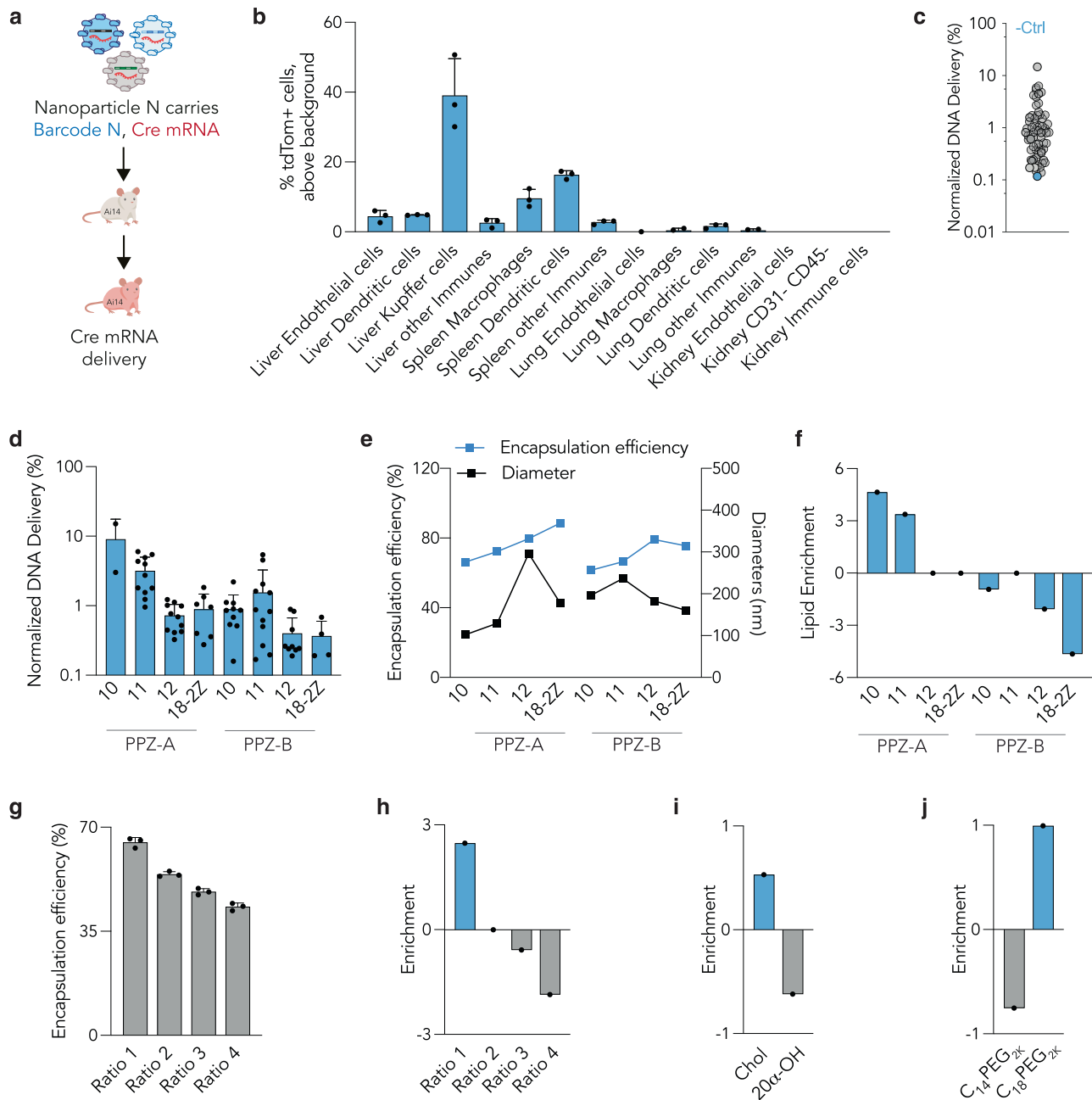


**Fig. 2 | Quantifying how 65 LNPs delivered mRNA delivery to 14 cell types in vivo, and subsequent in vivo structure-function analysis.** **a** LNPs were formulated to carry a unique DNA barcode and Cre mRNA. The 65 LNP pool was then administered to Ai14 mice. After 3 days %tdTomato+ cells were quantified in **b** multiple cell types in the liver, spleen, lung, and kidney (Average  $\pm$  SEM,  $N = 4$ /group). Source data are provided as a Source Data file. **c** Normalized delivery for all 65 LNPs, averaged across all samples. Unencapsulated DNA barcode, acting as a negative control (-Ctrl), was delivered into cells less efficiently than barcodes encapsulated by LNPs. **d** Normalized delivery of LNPs formulated with each PPZ

lipid, average  $\pm$  SD. **e** Encapsulation efficiencies and diameters for LNPs formulated with PPZ-A10, cholesterol, C18PEG2K, and DOPE at a ratio of 35:46.5:2.5:16. **f** Fold enrichment calculated based on different lipids. **g** Encapsulation efficiencies of LNPs formulated with PPZ-A10, cholesterol, C<sub>18</sub>PEG<sub>2K</sub>, DOPE at four molar ratios; ratio 1 = 30:30:1:39; ratio 2 = 35:46.5:2.5:16; ratio 3 = 45:39.5:2.5:13; ratio 4 = 50:35:2.5:12.5, average  $\pm$  SEM. **h** Fold enrichment calculated based on different ratios. **i** Fold enrichment calculated for cholesterol and 20 $\alpha$ -OH cholesterol. **j** Fold enrichment calculated for C<sub>14</sub>PEG<sub>2K</sub> and C<sub>18</sub>PEG<sub>2K</sub>.

complement this structure-function analysis, which included all tested Pi-LNPs, we analyzed the relationship between Pi-Lipid structure and in vivo activity using enrichment (Fig. 2f), which only includes the best and worst nanoparticles. Enrichment, which can be used to understand LNP structure function<sup>47,48</sup>, calculates the odds that a material is found in the top or bottom 10% of the LNPs, relative to random chance (Supplementary Fig. 4). Consistent with the normalized delivery data, enrichment analysis highlighted that PPZ-A scaffolds outperformed PPZ-B, and among all lipids, PPZ-A10

was the most enriched. Subsequently, we investigated how other material properties affected LNP delivery. We formulated four LNPs using PPZ-A10, cholesterol, C<sub>18</sub>PEG<sub>2K</sub>, and DOPE, varying only the molar ratio of each component, and measured the encapsulation efficiencies (Fig. 2g). Ratio 1, containing the lowest percentage of ionizable lipid and the highest percentage of DOPE, formulated with the highest encapsulation efficiency, whereas increasing the molar ratio of ionizable lipid, and therefore decreasing DOPE, resulted in a reduction of encapsulation efficiency. We then explored how these





50% tdTomato<sup>+</sup> Kupffer cells, 23% tdTomato<sup>+</sup> splenic macrophages, and 26% tdTomato<sup>+</sup> splenic dendritic cells, demonstrating that LNP-A10 can deliver mRNA-relevant payloads. Finally, we evaluated whether LNP-A10 delivered siRNA; notably, it can be difficult to identify a single nanoparticle that efficiently delivers both mRNA and siRNA, due to the distinct biophysical differences between the two payloads<sup>50</sup>. We therefore formulated LNP-A10 with siGFP as well as siLuciferase (siLuc) and injected it intravenously into GFP mice at a dose of 1 mg/kg. siLuc, an siRNA that does not interfere with GFP expression, was included as a control to eliminate the possibility of a toxicity-induced decrease in GFP protein expression. We observed about 25% silencing of GFP protein expression in Kupffer cells (Fig. 3f), whereas no silencing was observed in control mice injected with siLuc. This led us to conclude that LNP-A10 could also deliver siRNA, albeit with lower efficiency than mRNA.

## Discussion

By designing, synthesizing, and characterizing 128 novel Pi-LNPs, we found that Pi-Lipids can be formulated into stable nanoparticles, and that these nanoparticles can deliver nucleic acids to non-hepatocytes in vivo. Notably, the leading LNP, LNP-A10, that delivered mRNA preferentially to liver and spleen immune cells at a dose as low as 0.3 mg/kg, was identified directly using an in vivo barcoding approach, demonstrating the utility of direct in vivo high-throughput nanoparticle studies. We compared the structure of our PPZ-lipids with lipids that included a piperazine motif. When compared to C12-200<sup>39</sup>, we added amide bonds and removed hydroxyl groups. These hydroxyl can lead to stereoisomers, which can make purification difficult. By contrast, the PPZ-lipids are stereopure, which makes them easier to purify. These chemical changes may be responsible for the shift in tropism we noted; specifically, we found increased splenic macrophage and dendritic cell delivery, compared to previously reported C12-200 publications. We then compared the structure to C14-4, which was shown to deliver mRNA to Jurkat cells and primary human T cells in vitro<sup>51</sup>. However, it is difficult to compare in vitro and in vivo delivery<sup>29</sup>. One key limitation of this work is that LNP delivery may vary across species<sup>52</sup>, and thus, these results need to be confirmed in larger animals. Taken together, we believe the data justify further exploration of LNPs with piperazine rings.

## Methods

### Statistics & reproducibility

For in vivo experiments:  $N = 2$  for PBS negative control and 3 or 4 mice for experimental control. Those sample sizes were chosen to ensure the accuracy of the data and accurate statistics. The 2 mice per PBS control were chosen to limit the number of mice. No statistical method was used to predetermine sample size. No data were excluded from the analyses. Mice were randomly selected, and no algorithm was used. The Investigators were not blinded to allocation during experiments and outcome assessment.

### Nanoparticle formulation

Nanoparticles were formulated with a microfluidic device as previously described<sup>1</sup>. Nucleic acids (DNA barcodes and mRNA) were diluted in a 10 mM citrate buffer (Teknova). Lipid-amine compounds, PEG-lipids (1,2-dimyristoyl-sn-glycerol-3-phosphoethanolamine-N-[methoxy(polyethyleneglycol)-2000] and 1,2-distearoyl-sn-glycerol-3-phosphoethanolamine-N-[methoxy(polyethyleneglycol)-2000]), cholesterol (cholesterol and 20 $\alpha$ -OH cholesterol), and helper lipid 1,2-dioleoyl-sn-glycerol-3-phosphoethanolamine were diluted in 100% ethanol. Cre mRNA and DNA barcodes were mixed at a 10:1 mass ratio for mRNA screens. All PEGs, cholesterol, and helper lipids were purchased from Avanti Lipids. Citrate and ethanol phases were combined in a microfluidic device by syringes (Hamilton Company) at a flow rate of 3:1. The LNPs were dialyzed into 1 $\times$  PBS to remove the solvent.

### DNA barcoding

Each LNP was formulated to carry its own unique DNA barcode. DNA barcodes were designed rationally with several characteristics as described<sup>2</sup>. All DNA barcodes were 91-nt-long, single-stranded DNA sequences purchased from Integrated DNA Technologies. Briefly, the following modification was on all barcodes: (i) nucleotides on the 5' and 3' ends were modified with phosphorothioates to reduce exonuclease degradation (ii) universal forward and reverse primer regions were included to ensure equal amplification of each sequence, (iii) 7 random nucleotides were included to monitor PCR bias, (iv) a droplet digital PCR (ddPCR) probe site was included for ddPCR compatibility, and (v) a unique 8-nt barcode was assigned. An 8-nucleotide sequence can generate over 4 (65,536) distinct barcodes. We used only the 8-nucleotide sequences designed to prevent sequence bleaching and reading errors on the Illumina MiniSeq<sup>TM</sup> sequencing machine.

### Nanoparticle characterization

LNP hydrodynamic diameter was measured using high-throughput dynamic light scattering (DynaPro Plate Reader II, Wyatt). LNPs were diluted in sterile 1 $\times$  PBS and analyzed. To avoid using unstable LNPs, and to enable sterile purification using a 0.22  $\mu$ m filter, LNPs were included only if they met three criteria: diameter >20 nm, diameter <200 nm, and correlation function with 1 inflection point. Particles that met these criteria were pooled and dialyzed in a 20 kD dialysis cassette (Thermo Scientific) and a 100 kD cassette (Thermo Scientific) in 1 $\times$  PBS. The nanoparticle concentration was determined using NanoDrop (Thermo Scientific). LNP encapsulation was measured using a Quant-iT RiboGreen assay (Thermo Fisher)<sup>3</sup>.

### Animal experiments

All animal experiments were performed in accordance with the Georgia Institute of Technology's IACUC (protocol number A100238). All animals were bred in the Georgia Institute of Technology Animal Facility. C57BL/6J (#000664) were purchased from The Jackson Laboratory. LSL-Tomato/Ai14 (#007914) were purchased from The Jackson Laboratory for breeding purposes. All mice were 6 to 8 weeks old at the time of the experiments. In all experiments, we used  $N = 2-4$  mice/group. Mice were injected intravenously via the lateral tail vein. The nanoparticle concentration was determined using NanoDrop (Thermo Scientific). All animals were housed in the Georgia Institute of Technology Animal Facility.

### Cell isolation and staining

Cells were isolated 24 or 72 h after injection with LNPs, unless otherwise noted. Mice were perfused in the liver portal vein with 5 mL of Krebs Ringer buffer (pH 7.3). Tissues were finely minced and then placed in Collagenase XI (Sigma Aldrich) at 37  $^{\circ}$ C at 500 rpm for 30 min. The cell suspension was filtered through 70  $\mu$ m mesh and washed with 1 $\times$  PBS. Cells were stained to identify specific cell populations and sorted using the BD FACS Fusion cell sorter at the Georgia Institute of Technology Cellular Analysis Core. The antibody clones used were: Live/dead far-red fluorescent dye (Invitrogen, dilution 1:250), anti-mouse CD31 (390, BioLegend, dilution 1:250), anti-mouse CD45.2 (104, BioLegend, dilution 1:250), anti-mouse CD68 (FA11, BioLegend, dilution 1:250), anti-mouse CD11b (M1/70, BioLegend, dilution 1:250), anti-mouse CD11c (N418, BioLegend, dilution 1:250), anti-mouse CD3 (17A2, BioLegend, dilution 1:250), anti-mouse CD19 (6D5, BioLegend, dilution 1:250). Representative flow gates are in Supplementary Figs. 1 and 2. PBS-injected mice were used to gate on tdTomato positive populations.

### PCR amplification

All samples were amplified and prepared for sequencing using nested PCR<sup>4</sup>. More specifically, 1  $\mu$ L of primers (5  $\mu$ M for Final Reverse/Forward) were added to 5  $\mu$ L of Kapa HiFi 2 $\times$  master mix (Roche), and 4  $\mu$ L

template DNA/water. During the second PCR Nextera XT chemistry, indices and i5/i7 adapter regions were added. Dual-indexed samples were run on a 2% agarose gel to ensure that PCR reaction occurred before being pooled and gel purified. The primers used for the nested PCR are listed below, all primers were mixed in equal molar:

FWD_1	TCG TCG GCA GCG TCA GAT GTG TAT AAG AGA CAG GCT CTC ATA CGA ACT CGT CC
FWD_2	TCG TCG GCA GCG TCA GAT GTG TAT AAG AGA CAG TGC TCT CAT ACG AAC TCG TCC
FWD_3	TCG TCG GCA GCG TCA GAT GTG TAT AAG AGA CAG ATG CTC TCA TAC GAA CTC GTC C
FWD_4	TCG TCG GCA GCG TCA GAT GTG TAT AAG AGA CAG GAT GCT CTC ATA CGA ACT CGT CC
FWD_5	TCG TCG GCA GCG TCA GAT GTG TAT AAG AGA CAG CGA TGC TCT CAT ACG AAC TCG TCC
FWD_6	TCG TCG GCA GCG TCA GAT GTG TAT AAG AGA CAG TCG ATG CTC TCA TAC GAA CTC GTC C
FWD_7	TCG TCG GCA GCG TCA GAT GTG TAT AAG AGA CAG ATC GAT GCT CTC ATA CGA ACT CGT CC
FWD_8	TCG TCG GCA GCG TCA GAT GTG TAT AAG AGA CAG GAT CGA TGC TCT CAT ACG AAC TCG TCC
RVS_1	GTC TCG TGG GCT CGG AGA TGT GTA TAA GAG ACA GGT CTC TGC TCG ACT AAC CAC
RVS_2	GTC TCG TGG GCT CGG AGA TGT GTA TAA GAG ACA GTG TCT CTG CTC GAC TAA CCA C
RVS_3	GTC TCG TGG GCT CGG AGA TGT GTA TAA GAG ACA GAT GTC TCT GCT CGA CTA ACC AC
RVS_4	GTC TCG TGG GCT CGG AGA TGT GTA TAA GAG ACA GGA TGT CTC TCG TCG ACT AAC CAC
RVS_5	GTC TCG TGG GCT CGG AGA TGT GTA TAA GAG ACA GCG ATG TCT CTG CTC GAC TAA CCA C
RVS_6	GTC TCG TGG GCT CGG AGA TGT GTA TAA GAG ACA GTC GAT GTC TCT GCT CGA CTA ACC AC
RVS_7	GTC TCG TGG GCT CGG AGA TGT GTA TAA GAG ACA GAT CGA TGT CTC TGC TCG ACT AAC CAC
RVS_8	GTC TCG TGG GCT CGG AGA TGT GTA TAA GAG ACA GGA TCG ATG TCT CTG CTC GAC TAA CCA C

### Deep sequencing

PCR samples were purified by AMPure XP beads. Final library QC was conducted using the Agilent Bioanalyzer 2100. Illumina deep sequencing was conducted on an Illumina MiniSeq™. Primers were designed based on Nextera XT adapter sequences.

#### Illumina Index

Universal Reverse Primer ( N7XX)	AATGATACGGCGACCACCGAGATCTACACTAAGGCCA ACACTCTTTCCCTACACGACGCTCTTCCGATCT
Universal Forward Primer ( S5XX)	CAAGCAGAAGACGGCATACGAGATATAGAGACGTGAC TGGAGTTCCAGACGTGTG

Index Name	Index Sequence	Index Name	Index Sequence
N701	TAAGGCCA	S502	ATAGAGAG
N702	CGTACTAG	S503	AGAGGATA
N703	AGGCAGAA	S505	CTCCTTAC
N704	TCTTGAGC	S506	TATGCAGT
N705	GGACTCCT	S507	TACTCCTT
N706	TAGGCATG	S508	AGGCTTAG
N707	CTCTCTAC	S510	ATTAGACG
N710	CGAGGCTG	S511	CGGAGAGA
N711	AAGAGGCA	S513	CTAGTCGA
N712	GTAGAGGA	S515	AGCTAGAA
N714	GCTCATGA	S516	ACTCTAGG
N715	ATCTCAGG	S517	TCTTACGC
		S518	CTTAATAG
		S520	ATAGCCTT
		S521	TAAGGCTC
		S522	TCGCATAA

### Nanoparticle data analysis and statistics

Sequencing results were processed using a custom Python-based tool to extract raw barcode counts for each tissue. These raw counts were normalized with an R script before further analysis. Counts for each

particle, per tissue, were normalized to the barcoded LNP mixture injected into the mouse. This “input” DNA provided the DNA counts and was used to normalize DNA counts from the cells and tissues. Statistical analysis was done using GraphPad Prism 8. Data are plotted as mean ± standard error mean unless otherwise stated.

### Reporting summary

Further information on research design is available in the Nature Research Reporting Summary linked to this article.

### Data availability

Source data are provided with this manuscript. The scripts used to analyze DNA barcoding results are available online [[https://github.com/Jack-Feldman/barcode\\_count](https://github.com/Jack-Feldman/barcode_count)]. All other data are shown in the manuscript and Supporting Information. H.N., M.Z.C.H., and J.E.D. via the Georgia Institute of Technology Research Corporation, have filed a provisional patent application related to this technology (US patent provisional 63/293,287). Source data are provided with this paper.

### Code availability

All code used to analyze the data is available online [[https://github.com/Jack-Feldman/barcode\\_count](https://github.com/Jack-Feldman/barcode_count)].

### References

- Adams, D. et al. Patisiran, an RNAi therapeutic, for hereditary transthyretin amyloidosis. *N. Engl. J. Med.* **379**, 11–21 (2018).
- Nair, J. K. et al. Multivalent N-acetylgalactosamine-conjugated siRNA localizes in hepatocytes and elicits robust RNAi-mediated gene silencing. *J. Am. Chem. Soc.* **136**, 16958–16961 (2014).
- Balwani, M. et al. Phase 3 trial of RNAi therapeutic givosiran for acute intermittent porphyria. *N. Engl. J. Med.* **382**, 2289–2301 (2020).
- Ray, K. K. et al. Two phase 3 trials of inclisiran in patients with elevated LDL cholesterol. *N. Engl. J. Med.* **382**, 1507–1519 (2020).
- Garrelfs, S. F. et al. Lumasiran, an RNAi therapeutic for primary hyperoxaluria type 1. *N. Engl. J. Med.* **384**, 1216–1226 (2021).
- Polack, F. P. et al. Safety and efficacy of the BNT162b2 mRNA Covid-19 vaccine. *N. Engl. J. Med.* **383**, 2603–2615 (2020).
- Baden, L. R. et al. Efficacy and safety of the mRNA-1273 SARS-CoV-2 Vaccine. *New England J. Med.* (2020).
- Translate bio announces results from second interim data analysis from ongoing phase 1/2 clinical trial of MRT5005 in patients with cystic fibrosis (CF). <https://investors.translate.bio/news-releases/news-release-details/translate-bio-announces-results-second-interim-data-analysis>. (2021).
- Translate Bio Announces Pipeline Program Update. <https://investors.translate.bio/news-releases/news-release-details/translate-bio-announces-pipeline-program-update>. (2019).
- Loughrey, D. & Dahlman, J. E. Non-liver mRNA delivery. *Acc. Chem. Res.* **55**, 13–23 (2022).
- Lorenzer, C., Dirin, M., Winkler, A. M., Baumann, V. & Winkler, J. Going beyond the liver: progress and challenges of targeted delivery of siRNA therapeutics. *J. Controlled Release. Off. J. Controlled Release. Soc.* **203**, 1–15 (2015).
- Braet, F. & Wisse, E. Structural and functional aspects of liver sinusoidal endothelial cell fenestrae: a review. *Comp. Hepatol.* **1**, 1–1 (2002).
- Tsoi, K. M. et al. Mechanism of hard-nanomaterial clearance by the liver. *Nat. Mater.* **15**, 1212–1221 (2016).
- Paunovska, K., Loughrey, D. & Dahlman, J.E. Drug delivery systems for RNA therapeutics. *Nat. Rev. Genet.* **23**, 265–280 (2022).
- Saunders, N. R. M. et al. A nanoprimer to improve the systemic delivery of siRNA and mRNA. *Nano Lett.* **20**, 4264–4269 (2020).

16. Sago, C. D. et al. Augmented lipid-nanoparticle-mediated in vivo genome editing in the lungs and spleen by disrupting Cas9 activity in the liver. *Nat. Biomed. Eng.* **6**, 157–167 (2022).
17. Jayaraman, M. et al. Maximizing the potency of siRNA lipid nanoparticles for hepatic gene silencing in vivo. *Angew. Chem.* **51**, 8529–8533 (2012).
18. Akinc, A. et al. The Onpatro story and the clinical translation of nanomedicines containing nucleic acid-based drugs. *Nat. Nanotechnol.* **14**, 1084–1087 (2019).
19. Dammes, N. et al. Conformation-sensitive targeting of lipid nanoparticles for RNA therapeutics. *Nat. Nanotechnol.* **16**, 1030–1038 (2021).
20. Ramishetti, S. et al. A combinatorial library of lipid nanoparticles for RNA delivery to leukocytes. *Adv. Mater.* **32**, e1906128 (2020).
21. Kedmi, R. et al. A modular platform for targeted RNAi therapeutics. *Nat. Nanotechnol.* **13**, 214–219 (2018).
22. Veiga, N. et al. Cell specific delivery of modified mRNA expressing therapeutic proteins to leukocytes. *Nat. Commun.* **9**, 4493 (2018).
23. Zuckerman, J. E. et al. Correlating animal and human phase Ia/Ib clinical data with CALAA-01, a targeted, polymer-based nanoparticle containing siRNA. *Proc. Natl Acad. Sci. USA* **111**, 11449–11454 (2014).
24. Akinc, A. et al. Targeted delivery of RNAi therapeutics with endogenous and exogenous ligand-based mechanisms. *Mol. Ther.: J. Am. Soc. Gene Ther.* **18**, 1357–1364 (2010).
25. Gillmore, J.D. et al. CRISPR-Cas9 in vivo gene editing for transthyretin amyloidosis. *N Engl. J. Med.* **385**, 493–502 (2021).
26. Akinc, A. et al. A combinatorial library of lipid-like materials for delivery of RNAi therapeutics. *Nat. Biotechnol.* **26**, 561–569 (2008).
27. Dahlman, J. E. et al. In vivo endothelial siRNA delivery using polymeric nanoparticles with low molecular weight. *Nat. Nano* **9**, 648–655 (2014).
28. Siegwart, D. J. et al. Combinatorial synthesis of chemically diverse core-shell nanoparticles for intracellular delivery. *Proc. Natl Acad. Sci. USA* **108**, 12996–13001 (2011).
29. Paunovska, K. et al. A direct comparison of in vitro and in vivo nucleic acid delivery mediated by hundreds of nanoparticles reveals a weak correlation. *Nano Lett.* **18**, 2148–2157 (2018).
30. Lokugamage, M. P., Sago, C. D. & Dahlman, J. E. Testing thousands of nanoparticles in vivo using DNA barcodes. *Curr. Opin. Biomed. Eng.* **7**, 1–8 (2018).
31. Freitag, F. & Wagner, E. Optimizing synthetic nucleic acid and protein nanocarriers: the chemical evolution approach. *Adv. drug Deliv. Rev.* **168**, 30–54 (2021).
32. Sago, C.D. et al. High-throughput in vivo screen of functional mRNA delivery identifies nanoparticles for endothelial cell gene editing. *Proc. Natl Acad. Sci. USA* **115**, E9944–E9952 (2018).
33. Shaquiquzaman, M. et al. Piperazine scaffold: a remarkable tool in generation of diverse pharmacological agents. *Eur. J. medicinal Chem.* **102**, 487–529 (2015).
34. Magriotis, P. A. Recent progress toward the asymmetric synthesis of carbon-substituted piperazine pharmacophores and oxidative related heterocycles. *RSC Med Chem.* **11**, 745–759 (2020).
35. Chilmonczyk, Z., Krajewski, K. J. & Cybulski, J. Rigid analogues of buspirone and gepirone, 5-HT<sub>1A</sub> receptors partial agonists. *Farmaco* **57**, 917–923 (2002).
36. Fulton, A., Norman, T. & Burrows, G. D. Ligand binding and platelet uptake studies of loxapine, amoxapine and their 8-hydroxylated derivatives. *J. Affect Disord.* **4**, 113–119 (1982).
37. Sharma, P. C., Jain, A., Jain, S., Pahwa, R. & Yar, M. S. Ciprofloxacin: review on developments in synthetic, analytical, and medicinal aspects. *J. Enzym. Inhibition Med. Chem.* **25**, 577–589 (2010).
38. Girase, P. S. et al. An appraisal of anti-mycobacterial activity with structure-activity relationship of piperazine and its analogues: a review. *Eur. J. Med. Chem.* **210**, 112967 (2021).
39. Love, K. T. et al. Lipid-like materials for low-dose, in vivo gene silencing. *Proc. Natl Acad. Sci. USA* **107**, 1864–1869 (2010).
40. Semple, S. C. et al. Rational design of cationic lipids for siRNA delivery. *Nat. Biotechnol.* **28**, 172–176 (2010).
41. Fenton, O. S. et al. Bioinspired alkenyl amino alcohol ionizable lipid materials for highly potent in vivo mRNA delivery. *Adv. Mater.* **28**, 2939–2943 (2016).
42. Chen, D. et al. Rapid discovery of potent siRNA-containing lipid nanoparticles enabled by controlled microfluidic formulation. *J. Am. Chem. Soc.* **134**, 6948–6951 (2012).
43. Gan, Z. et al. Nanoparticles containing constrained phospholipids deliver mRNA to liver immune cells in vivo without targeting ligands. *Bioeng. Transl. Med* **5**, e10161 (2020).
44. Paunovska, K. et al. Nanoparticles containing oxidized cholesterol deliver mRNA to the liver microenvironment at clinically relevant doses. *Adv. Mater.*, e1807748 (2019).
45. Lokugamage, M. P. et al. Mild innate immune activation overrides efficient nanoparticle-mediated RNA delivery. *Adv. Mater.*, e1904905 (2019).
46. Akinc, A. et al. Development of lipidoid-siRNA formulations for systemic delivery to the liver. *Mol. Ther.: J. Am. Soc. Gene Ther.* **17**, 872–879 (2009).
47. Sago, C. D. et al. Nanoparticles that deliver RNA to bone marrow identified by in vivo directed evolution. *J. Am. Chem. Soc.* **140**, 17095–17105 (2018).
48. Paunovska, K. et al. Analyzing 2000 in vivo drug delivery data points reveals cholesterol structure impacts nanoparticle delivery. *ACS nano* **12**, 8341–8349 (2018).
49. Sago, C. D. et al. Modifying a commonly expressed endocytic receptor retargets nanoparticles in vivo. *Nano Lett.* **18**, 7590–7600 (2018).
50. Kauffman, K. J. et al. Optimization of lipid nanoparticle formulations for mRNA delivery in vivo with fractional factorial and definitive screening designs. *Nano Lett.* **15**, 7300–7306 (2015).
51. Billingsley, M. M. et al. Ionizable lipid nanoparticle-mediated mRNA delivery for human CAR T cell engineering. *Nano Lett.* **20**, 1578–1589 (2020).
52. Hatit, M. Z. C. et al. Species-dependent in vivo mRNA delivery and cellular responses to nanoparticles. *Nat. Nanotechnol.* **17**, 310–318 (2022).

## Acknowledgements

The work was funded by the National Institutes of Health (UG3-TRO02855, awarded to J.E.D. and P.J.S.) and DARPA (PREPARE grant number HRO011920008, awarded to P.J.S. and J.E.D.). We thank Karen E. Tiegren and Robert Hughley at Georgia Tech.

## Author contributions

H.N., M.Z.C.H., and J.E.D. conceived the experiments. P.J.S. and J.E.D. obtained funding for the research. H.N., M.Z.C.H., K.Z., D.L., M.P.L., H.E.P., A.D.C., A.M., and Y.K., performed the experiments. H.N., M.Z.C.H., and J.E.D. wrote the initial manuscript, which was edited by the other authors.

## Competing interests

H.N., M.Z.C.H., and J.E.D. have filed intellectual property related to this manuscript (US patent provisional 63/293,287). J.E.D. is an advisor to GV. All other authors declare no competing interests.



## Additional information

**Supplementary information** The online version contains supplementary material available at <https://doi.org/10.1038/s41467-022-32281-5>.

**Correspondence** and requests for materials should be addressed to James E. Dahlman.

**Peer review information** *Nature Communications* thanks the anonymous, reviewer(s) for their contribution to the peer review of this work.

**Reprints and permission information** is available at <http://www.nature.com/reprints>

**Publisher's note** Springer Nature remains neutral with regard to jurisdictional claims in published maps and institutional affiliations.

**Open Access** This article is licensed under a Creative Commons Attribution 4.0 International License, which permits use, sharing, adaptation, distribution and reproduction in any medium or format, as long as you give appropriate credit to the original author(s) and the source, provide a link to the Creative Commons license, and indicate if changes were made. The images or other third party material in this article are included in the article's Creative Commons license, unless indicated otherwise in a credit line to the material. If material is not included in the article's Creative Commons license and your intended use is not permitted by statutory regulation or exceeds the permitted use, you will need to obtain permission directly from the copyright holder. To view a copy of this license, visit <http://creativecommons.org/licenses/by/4.0/>.

© The Author(s) 2022